

Chapter 2

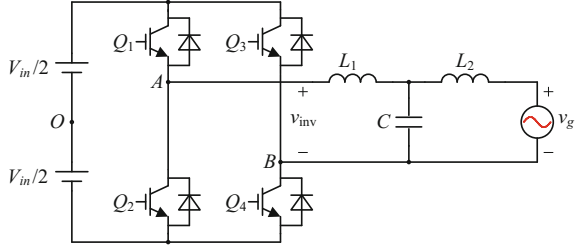
Design of *LCL* Filter

Abstract As the interface between renewable energy power generation system and the power grid, the grid-connected inverter is used to convert the dc power to the high-quality ac power and feed it into the power grid. In the grid-connected inverter, a filter is needed as the interface between the inverter and the power grid. Compared with the *L* filter, the *LCL* filter is considered to be a preferred choice for its cost-effective attenuation of switching frequency harmonics in the injected grid currents. To achieve high-quality grid current, the *LCL* filter should be properly designed. In this chapter, the widely used pulse-width modulation (PWM) schemes are introduced, including the bipolar sinusoidal pulse-width modulation (SPWM), unipolar SPWM and harmonic injection SPWM. The spectrums of the output PWM voltage with different SPWM are studied and compared. A design procedure for *LCL* filter based on the restriction standards of injected grid current is presented and verified by simulations.

Keywords Grid-connected inverter • *LCL* filter • Pulse-width modulation (PWM) • Total harmonics distortion (THD)

As the interface between renewable energy power generation system and the power grid, the grid-connected inverter is used to convert the dc power to the high-quality ac power and feed it into the power grid. In the grid-connected inverter, a filter is needed as the interface between the inverter and the power grid. Compared with the *L* filter, the *LCL* filter is considered to be a preferred choice for its cost-effective attenuation of switching frequency harmonics in the injected grid currents. To achieve high-quality grid current, the *LCL* filter should be properly designed. In this chapter, the widely used pulse-width modulation (PWM) schemes are introduced, including the bipolar sinusoidal pulse-width modulation (SPWM), unipolar SPWM and harmonic injection SPWM. The spectrums of the output PWM voltage with different SPWM are studied and compared. A design procedure for *LCL* filter based on the restriction standards of injected grid current is presented and verified by simulations.

Fig. 2.1 Single-phase *LCL*-type grid-connected inverter



2.1 PWM for Single-Phase Full-Bridge Grid-Connected Inverter

Figure 2.1 shows the topology of a single-phase full-bridge *LCL*-type grid-connected inverter, where switches Q_1 – Q_4 compose the two bridge legs, and inductors L_1 , L_2 and capacitor C compose the *LCL* filter. Note that the two switches in the same bridge leg are switched in a complementary manner.

Generally, the bipolar SPWM and unipolar SPWM are usually used for single-phase full-bridge inverter. For convenience of illustration, the dc input voltage V_{in} is split into two ones equally, and the midpoint O is defined as the base potential.

2.1.1 Bipolar SPWM

Figure 2.2 shows the key waveforms of the bipolar SPWM for single-phase *LCL*-type grid-connected inverter, where, v_M is the sinusoidal modulation signal with the amplitude of V_M , and v_{tri} is the triangular carrier with the amplitude of V_{tri} . When $v_M > v_{tri}$, Q_1 and Q_4 turn on, Q_2 and Q_3 turn off, resulting in $v_{AO} = V_{in}/2$ and $v_{BO} = -V_{in}/2$; When $v_M < v_{tri}$, Q_1 and Q_4 turn off, Q_2 , Q_3 turn on, resulting in $v_{AO} = -V_{in}/2$ and $v_{BO} = V_{in}/2$. The inverter bridge output voltage v_{inv} is the difference between v_{AO} and v_{BO} , i.e., $v_{inv} = v_{AO} - v_{BO}$. As shown in Fig. 2.2, v_{inv} has only two voltage levels, namely $-V_{in}$ and $+V_{in}$. So, this PWM scheme is often called as bipolar SPWM.

In the following, ω_o and ω_{sw} denote the angular frequencies of the modulation signal v_M and triangular carrier v_{tri} , respectively, the initial phase of the modulation signal v_M is set to 0, and M_r denotes the ratio of V_M and V_{tri} , i.e.,

$$M_r = V_M/V_{tri} \quad (2.1)$$

According to the Fourier transform theory, the time-varying signals v_{AO} and v_{BO} shown in Fig. 2.2 can be expressed as [1]

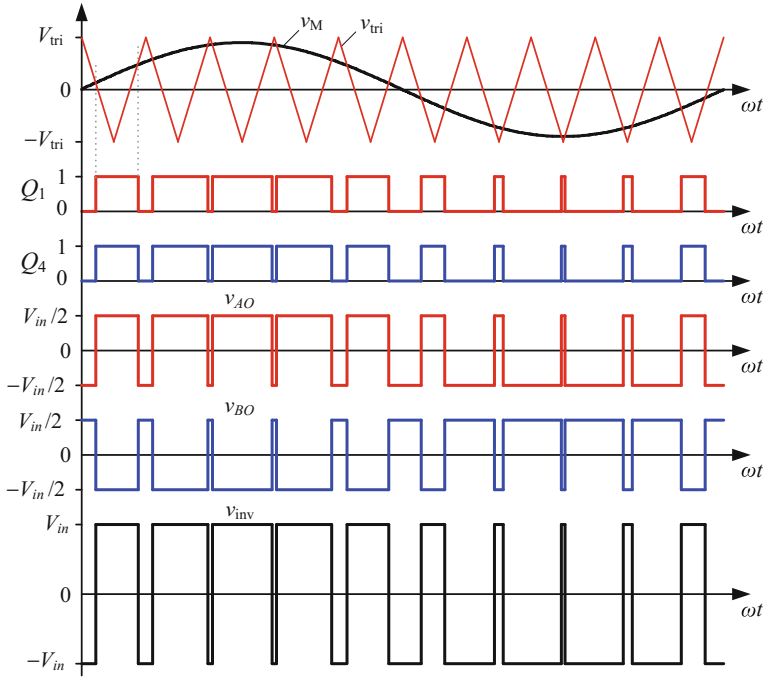


Fig. 2.2 Bipolar SPWM for single-phase *LCL*-type grid-connected inverter

$$\begin{aligned}
 v_{AO}(t) &= -v_{BO}(t) \\
 &= \frac{M_r V_{in}}{2} \sin \omega_o t + \frac{2V_{in}}{\pi} \sum_{m=1,3,\dots}^{\infty} \sum_{n=0,\pm 2,\pm 4,\dots}^{\pm \infty} \frac{J_n(mM_r\pi/2)}{m} \sin \frac{m\pi}{2} \cos(m\omega_{sw}t + n\omega_o t) \\
 &\quad + \frac{2V_{in}}{\pi} \sum_{m=2,4,\dots}^{\infty} \sum_{n=\pm 1,\pm 3,\dots}^{\pm \infty} \frac{J_n(mM_r\pi/2)}{m} \cos \frac{m\pi}{2} \sin(m\omega_{sw}t + n\omega_o t)
 \end{aligned} \tag{2.2}$$

where, $J_n(x)$ is the Bessel function of the first kind [2], expressed as

$$J_n(x) = \sum_{k=0}^{\infty} \frac{(-1)^k}{k!(k+n)!} \left(\frac{x}{2}\right)^{2k+n} \tag{2.3}$$

According to (2.2), the Fourier series expansion of the inverter bridge output voltage v_{inv} with bipolar SPWM can be obtained, which is

$$\begin{aligned}
v_{inv}(t) &= v_{AO}(t) - v_{BO}(t) \\
&= M_r V_{in} \sin \omega_o t + \frac{4V_{in}}{\pi} \sum_{m=1,3,5,\dots}^{\infty} \sum_{n=0,\pm 2,\pm 4,\dots}^{\pm \infty} \frac{J_n(mM_r\pi/2)}{m} \sin \frac{m\pi}{2} \cos(m\omega_{sw}t + n\omega_o t) \\
&\quad + \frac{4V_{in}}{\pi} \sum_{m=2,4,6,\dots}^{\infty} \sum_{n=\pm 1,\pm 3,\dots}^{\pm \infty} \frac{J_n(mM_r\pi/2)}{m} \cos \frac{m\pi}{2} \sin(m\omega_{sw}t + n\omega_o t)
\end{aligned} \tag{2.4}$$

where, the first term is the fundamental component, the second term is the sideband harmonics around odd multiples of the carrier frequency, and the third term is the sideband harmonics around even multiples of the carrier frequency. In the second and third terms, m is the carrier index variable, and n is the baseband index variable. m and n determine the harmonics distribution. When m is odd, $|\sin(m\pi/2)| = 1$; When m is even, $|\cos(m\pi/2)| = 1$. With a given V_{in} , the amplitudes of the harmonics in v_{inv} are determined by $|J_n(mM_r\pi/2)/m|$. Moreover, the harmonics in v_{inv} distribute only at the frequencies where $m + n$ is odd.

According to (2.3), an example of $|J_n(mM_r\pi/2)/m|$ with $M_r = 0.9$ and $m = 1, 2$ and 3 is depicted with the dots, as shown in Fig. 2.3, where the three dashed lines are plotted with Gamma Function $\Gamma(k + n + 1)$, where the variable n uses a real number. As observed, the dot with the maximum value locates at the center frequency ω_{sw} , where $m = 1, n = 0$; the farther the sideband harmonic departs from the center frequency, the smaller its amplitude is. In contrast to the harmonics around the center frequency ω_{sw} , the amplitudes of the harmonics around twice and above the carrier frequency are much smaller. Thus, the dominant harmonics in v_{inv} are at around ω_{sw} , which needs to be attenuated by the LCL filter.

In conclusion, the spectrum of the inverter bridge output voltage, v_{inv} , generated by the bipolar SPWM can be described as

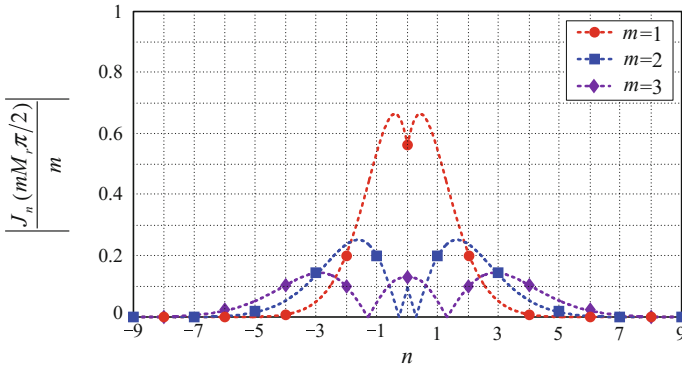


Fig. 2.3 Characteristic curves of Bessel function

- (1) The harmonics in v_{inv} distribute only at frequencies where $m + n$ is odd. When m is odd, the harmonics distribute not only at m times of the carrier frequency, but also at the sideband frequency when n is even; When m is even, the harmonics only distribute at the sideband frequency when n is odd;
- (2) The dominant harmonics in v_{inv} are at around the carrier frequency (e.g., $n = 0, \pm 2, \pm 4, \dots$). The design of the *LCL* filter is determined by attenuating these dominant harmonics.

2.1.2 Unipolar SPWM

As mentioned above, with the bipolar SPWM, the voltage levels of v_{inv} could only be $-V_{in}$ and $+V_{in}$. In fact, when Q_1 and Q_3 or Q_2 and Q_4 turn on simultaneously, v_{inv} will be 0. The unipolar SPWM is such a kind of the modulation scheme that could make v_{inv} be not only $+V_{in}$ and $-V_{in}$, but also 0.

Figure 2.4 shows the key waveforms of the unipolar SPWM for single-phase *LCL*-type grid-connected inverter, where v_M is the sinusoidal modulation signal, and v_{tri} and $-v_{tri}$ are the two sets of triangular carrier. Comparison of v_M and v_{tri} leads to the control signals for Q_1 and Q_2 , and comparison of v_M and $-v_{tri}$ leads to the control signals for Q_3 and Q_4 . In detail, when $v_M > v_{tri}$, Q_1 turns on and Q_2 turns off, thus $v_{AO} = V_{in}/2$; When $v_M < v_{tri}$, Q_1 turns off and Q_2 turns on, thus $v_{AO} = -V_{in}/2$. Likewise, when $v_M > -v_{tri}$, Q_4 turns on and Q_3 turns off, thus $v_{BO} = -V_{in}/2$; When $v_M < -v_{tri}$, Q_4 turns off and Q_3 turns on, thus $v_{BO} = V_{in}/2$. Since $v_{inv} = v_{AO} - v_{BO}$, the voltage levels of v_{inv} could be $+V_{in}$, $-V_{in}$, and 0. In the positive period of v_M , the voltage levels of v_{inv} could only be $+V_{in}$ and 0; while in the negative period of v_M , the voltage levels of v_{inv} could only be $-V_{in}$ and 0. Therefore, this modulation scheme is called unipolar SPWM. Furthermore, the ripple frequency of v_{inv} is twice the carrier frequency.

Since the control signal for Q_1 is obtained by comparing v_M and v_{tri} , the Fourier series expansion of v_{AO} is the same as (2.2). The control signal for Q_4 is obtained by comparing v_M and $-v_{tri}$, and $-v_{tri}$ lags v_{tri} with a phase of π , the Fourier series expansion of v_{BO} can be obtained by replacing $\omega_{sw}t$ in (2.2) with $\omega_{sw}t - \pi$. Thus, v_{BO} is expressed as

$$\begin{aligned}
 v_{BO}(t) = & -\frac{M_r V_{in}}{2} \sin \omega_o t \\
 & - \frac{2V_{in}}{\pi} \sum_{m=1,3,5,\dots}^{\infty} \sum_{n=0,\pm 2,\pm 4,\dots}^{\pm \infty} \frac{J_n(mM_r\pi/2)}{m} \sin \frac{m\pi}{2} \cos(m(\omega_{sw}t - \pi) + n\omega_o t) \\
 & - \frac{2V_{in}}{\pi} \sum_{m=2,4,6,\dots}^{\infty} \sum_{n=\pm 1,\pm 3,\dots}^{\pm \infty} \frac{J_n(mM_r\pi/2)}{m} \cos \frac{m\pi}{2} \sin(m(\omega_{sw}t - \pi) + n\omega_o t)
 \end{aligned} \tag{2.5}$$

Equation (2.5) can be further simplified as

$$\begin{aligned}
 v_{BO}(t) = & -\frac{M_r V_{in}}{2} \sin \omega_o t + \frac{2V_{in}}{\pi} \sum_{m=1,3,5,\dots}^{\infty} \sum_{n=0,\pm 2,\pm 4,\dots}^{\pm \infty} \frac{J_n(mM_r \pi/2)}{m} \sin \frac{m\pi}{2} \cos(m\omega_{sw}t + n\omega_o t) \\
 & - \frac{2V_{in}}{\pi} \sum_{m=2,4,6,\dots}^{\infty} \sum_{n=\pm 1,\pm 3,\dots}^{\pm \infty} \frac{J_n(mM_r \pi/2)}{m} \cos \frac{m\pi}{2} \sin(m\omega_{sw}t + n\omega_o t)
 \end{aligned} \quad (2.6)$$

According to (2.2) and (2.6), the Fourier series expansion of v_{inv} with the unipolar SPWM is expressed as

$$\begin{aligned}
 v_{inv}(t) &= v_{AO}(t) - v_{BO}(t) \\
 &= M_r V_{in} \sin \omega_o t + \frac{4V_{in}}{\pi} \sum_{m=2,4,6,\dots}^{\infty} \sum_{n=\pm 1,\pm 3,\dots}^{\pm \infty} \frac{J_n(mM_r \pi/2)}{m} \cos \frac{m\pi}{2} \sin(m\omega_{sw}t + n\omega_o t)
 \end{aligned} \quad (2.7)$$

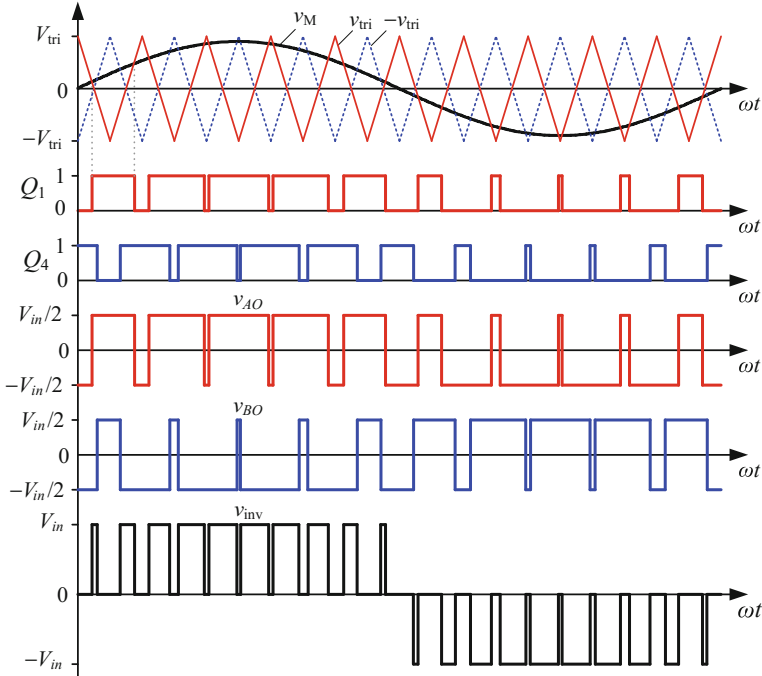


Fig. 2.4 Unipolar SPWM for single-phase *LCL*-type grid-connected inverter

According to (2.7), the harmonic spectrum of v_{inv} with the unipolar SPWM can be described as

- (1) The harmonics in v_{inv} distribute only at the sideband frequencies where m is even and n is odd.
- (2) The dominant harmonics in v_{inv} are at around twice the carrier frequency, which is the major consideration of filter design.

Comparing (2.4) and (2.7), it shows that the frequencies of the harmonics in v_{inv} with the unipolar SPWM are twice that of those with the bipolar SPWM. This is because the ripple frequencies of v_{inv} with the bipolar and unipolar SPWMs are one and two times of the carrier frequency, respectively, which can be found from Figs. 2.2 and 2.4.

2.2 PWM for Three-Phase Grid-Connected Inverter

Figure 2.5a shows the topology of a three-phase grid-connected inverter, where switches Q_1 – Q_6 compose the three-phase legs, and three sets of inductors L_1 , L_2 , and capacitor C compose the three-phase LCL filter. Note that the three-phase capacitors in LCL filter can be either delta- or star-connection. The capacitance needed in delta-connection is one-third of that in star-connection, and the capacitor

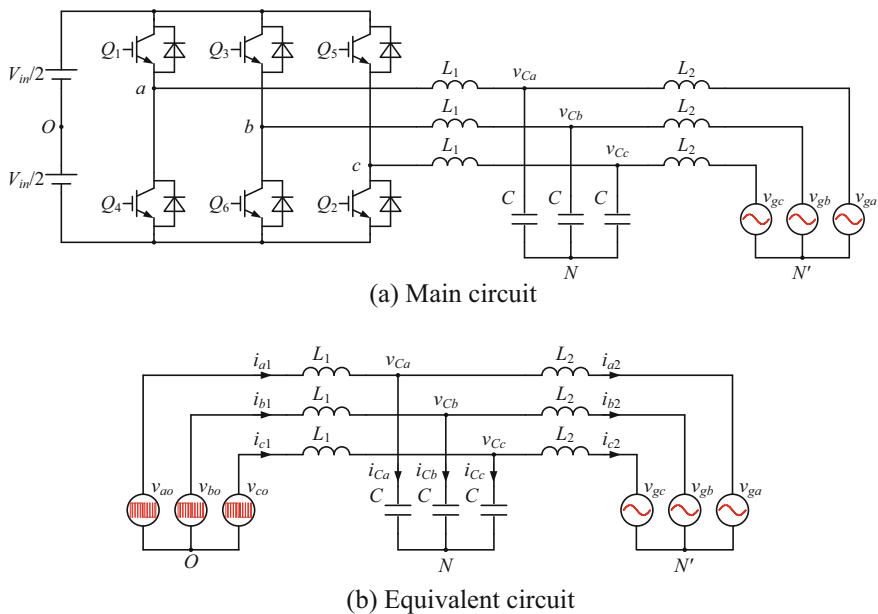


Fig. 2.5 Three-phase LCL -type grid-connected inverter

current and voltage stresses in delta-connection are $1/\sqrt{3}$ and $\sqrt{3}$ times of that in star-connection, respectively. In this book, star-connection is adopted. Similarly, V_{in} is split into two ones equally for convenience of illustration, and the midpoint O is defined as the base potential.

Figure 2.5b shows the equivalent circuit of the three-phase grid-connected inverter, where v_{ao} , v_{bo} , and v_{co} are the three inverter bridge output voltages with respect to midpoint O ; i_{1x} ($x = a, b, c$) is the inverter-side inductor current; v_{Cx} and i_{Cx} are the filter capacitor voltage and current, respectively; i_{2x} is the grid-side inductor current. From Fig. 2.5b, v_{ao} , v_{bo} and v_{co} can be expressed as

$$\begin{cases} v_{ao} = j\omega L_1 \cdot i_{1a} + v_{Ca} + v_{NO} \\ v_{bo} = j\omega L_1 \cdot i_{1b} + v_{Cb} + v_{NO} \\ v_{co} = j\omega L_1 \cdot i_{1c} + v_{Cc} + v_{NO} \end{cases} \quad (2.8)$$

where v_{NO} is the voltage across points N and O .

The three-phase filter capacitor voltages can be expressed as

$$\begin{cases} v_{Ca} = i_{Ca}/(j\omega C) \\ v_{Cb} = i_{Cb}/(j\omega C) \\ v_{Cc} = i_{Cc}/(j\omega C) \end{cases} \quad (2.9)$$

For three-phase three-wire system, $i_{1a} + i_{1b} + i_{1c} = 0$, $i_{Ca} + i_{Cb} + i_{Cc} = 0$. According to (2.8), the zero sequence component v_{NO} is derived as

$$v_{NO} = (v_{ao} + v_{bo} + v_{co})/3 \quad (2.10)$$

Similarly, $v_{NN'}$, the voltage across points N and N' , can be obtained, expressed as

$$v_{NN'} = (v_{ga} + v_{gb} + v_{gc})/3 \quad (2.11)$$

With PWM control, $v_{ao} + v_{bo} + v_{co} \neq 0$. So, according to (2.10), v_{NO} is not equal to zero, which means that the potentials of N and O are not equal. When the three-phase grid voltages are balance, i.e., $v_{ga} + v_{gb} + v_{gc} = 0$, the potentials of N and N' are equal according to (2.11).

2.2.1 SPWM

Figure 2.6 shows the key waveforms of SPWM for three-phase grid-connected inverter, where v_{tri} is the triangular carrier, and v_{Ma} , v_{Mb} , and v_{Mc} are the three-phase sinusoidal modulation signals, expressed as

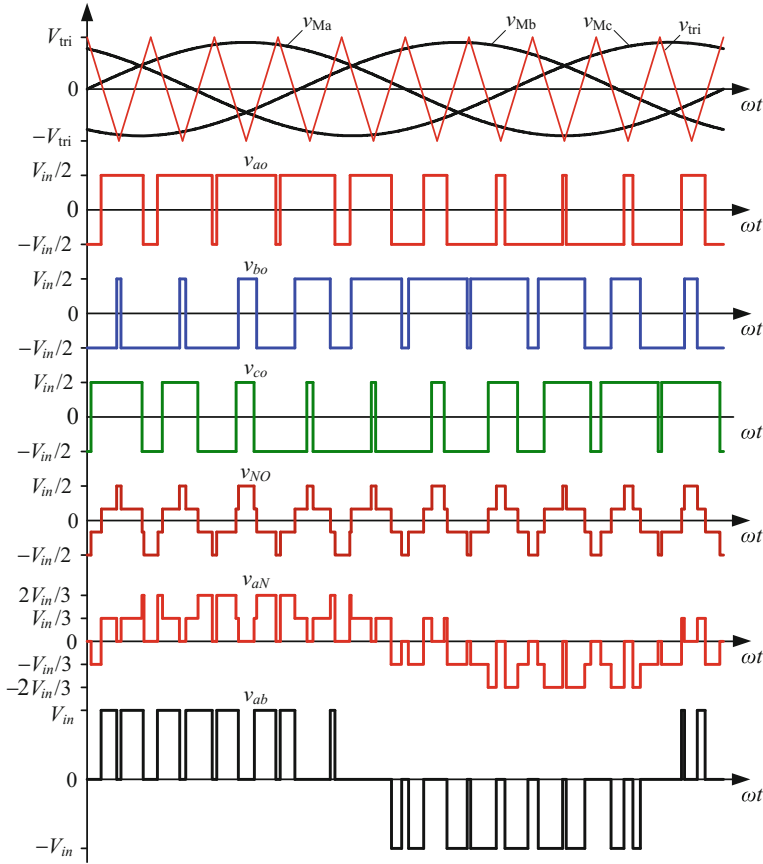


Fig. 2.6 SPWM for three-phase LCL-type grid-connected inverter

$$\begin{cases} v_{Ma} = V_M \cdot \sin \omega_o t \\ v_{Mb} = V_M \cdot \sin(\omega_o t - 2\pi/3) \\ v_{Mc} = V_M \cdot \sin(\omega_o t + 2\pi/3) \end{cases} \quad (2.12)$$

where V_M is the amplitude of the modulation signals, ω_o is the angular frequency of the modulation signals, which is equal to the grid angular frequency.

Obviously, the control signals for Q_1 and Q_4 are determined by comparing v_{Ma} and v_{tri} , the control signals for Q_3 and Q_6 are determined by comparing v_{Mb} and v_{tri} , and the control signals for Q_5 and Q_2 are determined by comparing v_{Mc} and v_{tri} . Thus, the voltages of the midpoints of three-phase legs with respect to O , v_{ao} , v_{bo} , and v_{co} , are obtained. v_{NO} can be determined according to (2.10). The output phase voltage v_{aN} is equal to $v_{ao} - v_{No}$, and the output line voltage v_{ab} is equal to $v_{ao} - v_{bo}$.

According to the modulation scheme, the expression of v_{ao} is the same as (2.2). Since v_{Mb} lags v_{Ma} with a phase of $2\pi/3$ and v_{Mc} leads v_{Ma} with a phase of $2\pi/3$, by replacing $\omega_o t$ in (2.2) with $\omega_o t - 2\pi/3$ and $\omega_o t + 2\pi/3$, respectively, the expressions of v_{bo} and v_{co} can be obtained as

$$\begin{aligned}
 v_{bo}(t) = & \frac{M_r V_{in}}{2} \sin\left(\omega_o t - \frac{2\pi}{3}\right) \\
 & + \frac{2V_{in}}{\pi} \sum_{m=1,3,\dots}^{\infty} \sum_{n=0,\pm 2,\dots}^{\pm\infty} \frac{J_n(mM_r\pi/2)}{m} \sin \frac{m\pi}{2} \cos\left(m\omega_{sw}t + n\left(\omega_o t - \frac{2\pi}{3}\right)\right) \\
 & + \frac{2V_{in}}{\pi} \sum_{m=2,4,\dots}^{\infty} \sum_{n=\pm 1,\pm 3,\dots}^{\pm\infty} \frac{J_n(mM_r\pi/2)}{m} \cos \frac{m\pi}{2} \sin\left(m\omega_{sw}t + n\left(\omega_o t - \frac{2\pi}{3}\right)\right)
 \end{aligned} \tag{2.13}$$

$$\begin{aligned}
 v_{co}(t) = & \frac{M_r V_{in}}{2} \sin\left(\omega_o t + \frac{2\pi}{3}\right) \\
 & + \frac{2V_{in}}{\pi} \sum_{m=1,3,\dots}^{\infty} \sum_{n=0,\pm 2,\dots}^{\pm\infty} \frac{J_n(mM_r\pi/2)}{m} \sin \frac{m\pi}{2} \cos\left(m\omega_{sw}t + n\left(\omega_o t + \frac{2\pi}{3}\right)\right) \\
 & + \frac{2V_{in}}{\pi} \sum_{m=2,4,\dots}^{\infty} \sum_{n=\pm 1,\pm 3,\dots}^{\pm\infty} \frac{J_n(mM_r\pi/2)}{m} \cos \frac{m\pi}{2} \sin\left(m\omega_{sw}t + n\left(\omega_o t + \frac{2\pi}{3}\right)\right)
 \end{aligned} \tag{2.14}$$

Substituting (2.2), (2.13), and (2.14) into (2.10) yields

$$\begin{aligned}
 v_{NO}(t) = & \frac{2V_{in}}{3\pi} \sum_{m=1,3,\dots}^{\infty} \sum_{n=0,\pm 2,\dots}^{\pm\infty} \frac{J_n(mM_r\pi/2)}{m} \left(1 + 2 \cos \frac{2n\pi}{3}\right) \sin \frac{m\pi}{2} \cos(m\omega_{sw}t + n\omega_o t) \\
 & + \frac{2V_{in}}{3\pi} \sum_{m=2,4,\dots}^{\infty} \sum_{n=\pm 1,\pm 3,\dots}^{\pm\infty} \frac{J_n(mM_r\pi/2)}{m} \left(1 + 2 \cos \frac{2n\pi}{3}\right) \cos \frac{m\pi}{2} \sin(m\omega_{sw}t + n\omega_o t)
 \end{aligned} \tag{2.15}$$

According to (2.2) and (2.15), the output phase voltage v_{aN} is obtained, which is

$$\begin{aligned}
 v_{aN}(t) = & v_{ao}(t) - v_{NO}(t) \\
 = & \frac{M_r V_{in}}{2} \sin \omega_o t + \frac{2V_{in}}{\pi} \sum_{m=1,3,5,\dots}^{\infty} \sum_{n=0,\pm 2,\pm 4,\dots}^{\pm\infty} \frac{4J_n(mM_r\pi/2)}{3} \frac{\sin \frac{m\pi}{2}}{m} \sin^2 \frac{n\pi}{3} \cos(m\omega_{sw}t + n\omega_o t) \\
 & + \frac{2V_{in}}{\pi} \sum_{m=2,4,6,\dots}^{\infty} \sum_{n=\pm 1,\pm 3,\dots}^{\pm\infty} \frac{4J_n(mM_r\pi/2)}{3} \frac{\cos \frac{m\pi}{2}}{m} \sin^2 \frac{n\pi}{3} \sin(m\omega_{sw}t + n\omega_o t)
 \end{aligned} \tag{2.16}$$

As seen in (2.16), for the harmonics in v_{aN} at around odd times ($m = 1, 3, 5, \dots$) of carrier frequency, when $n = 6k$ (k is an integer), $\sin^2(n\pi/3) = 0$; when $n = 6k \pm 2$, $\sin^2(n\pi/3) = 3/4$. Similarly, for the harmonics in v_{aN} at around even times ($m = 2, 4, 6, \dots$) of carrier frequency, when $n = 3(2k - 1)$, $\sin^2(n\pi/3) = 0$; when $n = 6k \pm 1$, $\sin^2(n\pi/3) = 3/4$.

So, the harmonics spectrum of the output phase voltages of three-phase inverter controlled by SPWM can be described as

- (1) The harmonics in the output phase voltages v_{xN} ($x = a, b, c$) only distribute at frequencies where $m + n$ is odd. When m is odd, the harmonics only distribute at the sideband frequencies where $n = 6k \pm 2$ (k is an integer); when m is even, the harmonics only distribute at the sideband frequencies where $n = 6k \pm 1$.
- (2) The harmonics in the output phase voltages v_{xN} at around the carrier frequency ($n = \pm 2, \pm 4, \dots$) are the dominant harmonics, which is the major consideration of filter design.

According to (2.2) and (2.13), the output line voltage v_{ab} can be obtained, expressed as

$$\begin{aligned}
 v_{ab}(t) &= v_{ao}(t) - v_{bo}(t) \\
 &= \frac{\sqrt{3}M_r V_{in}}{2} \sin\left(\omega_o t + \frac{\pi}{6}\right) \\
 &\quad + \frac{2V_{in}}{\pi} \sum_{m=1,3,5,\dots}^{\infty} \sum_{n=0,\pm 2,\pm 4,\dots}^{\pm\infty} \frac{J_n(mM_r\pi/2)}{m} \sin\frac{m\pi}{2} 2 \sin\frac{n\pi}{3} \cos\left(m\omega_{sw}t + n\omega_o t + \frac{\pi}{2} - \frac{n\pi}{3}\right) \\
 &\quad + \frac{2V_{in}}{\pi} \sum_{m=2,4,6,\dots}^{\infty} \sum_{n=\pm 1,\pm 3,\dots}^{\pm\infty} \frac{J_n(mM_r\pi/2)}{m} \cos\frac{m\pi}{2} 2 \sin\frac{n\pi}{3} \sin\left(m\omega_{sw}t + n\omega_o t + \frac{\pi}{2} - \frac{n\pi}{3}\right)
 \end{aligned} \tag{2.17}$$

By comparing (2.16) and (2.17), it can be observed that: (1) at the fundamental frequency, the amplitude of line voltage is $\sqrt{3}$ times of that of the phase voltage, and the line voltage leads to the phase voltage with a phase of $\pi/6$; (2) The harmonics of the output phase and line voltages v_{aN} and v_{ab} distribute at the same sideband frequencies, and the amplitudes of harmonics in line voltages are also $\sqrt{3}$ times of that of the harmonics in phase voltages, and it leads to the harmonics in the corresponding phase voltages with a phase of $\pi/2 - n\pi/3$.

2.2.2 Harmonic Injection SPWM Control

According to (2.17), when $0 \leq M_r \leq 1$, the maximum amplitude of output line voltage v_{ab} is only $\sqrt{3}V_{in}/2$, i.e., $0.866V_{in}$. It means that the dc voltage utilization of the three-phase inverter controlled by SPWM is only 0.866. However, according to (2.3) and (2.7), the dc voltage utilization of a single-phase full-bridge inverter is 1.

To make the dc voltage utilization of three-phase inverter attain 1, a third harmonic component v_z as shown in Fig. 2.7 is injected to the three-phase sinusoidal modulation signals. It can be observed that the peak of v_{Ma} and the valley of v_z appear at the same time. As a result, the peak of the modulation signal v_{Maz} , which is the sum of v_{Ma} and v_z , distributes not at but on both sides of the peak of v_{Ma} . When the amplitude of v_{Maz} is equal to that of v_{tri} , the real amplitude of v_{Ma} will be larger than that of v_{tri} . Define the modulation ratio of three-phase inverter is still the ratio of the amplitudes of v_{Ma} and v_{tri} , then according to (2.1), the modulation ratio larger than 1 will be obtained.

Further study shows that when the amplitude of the injected third harmonic component v_z is one-sixth of that of modulation sinusoidal signal v_{Ma} [1], i.e.,

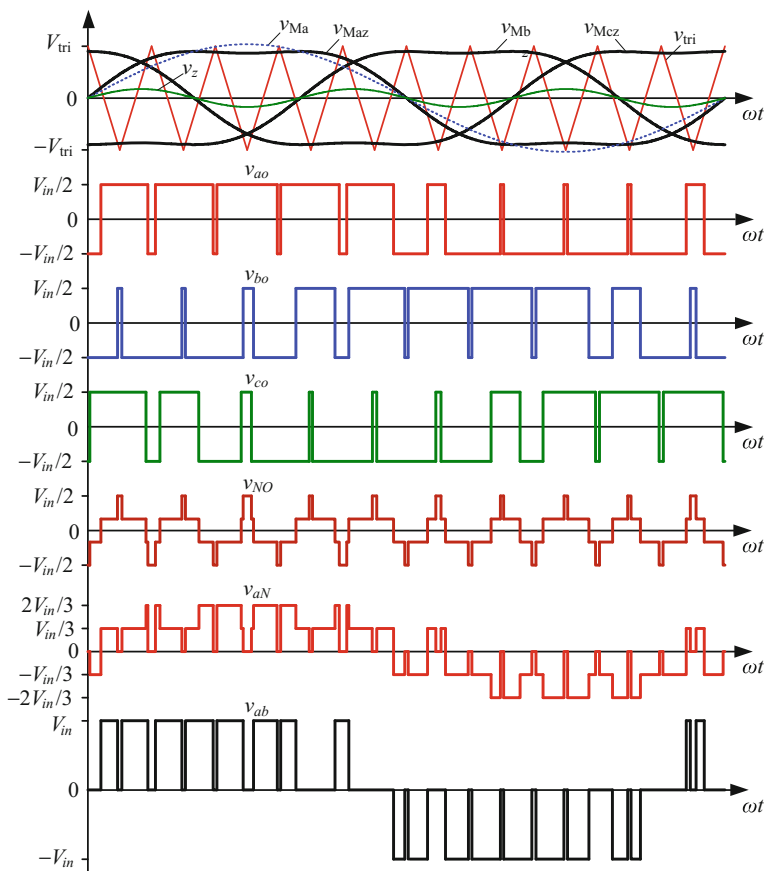


Fig. 2.7 Third harmonic injection SPWM for three-phase *LCL*-type grid-connected inverter

$$v_z = \frac{V_M}{6} \cdot \sin 3\omega_o t \quad (2.18)$$

the dc voltage utilization of the three-phase inverter attains 1. A brief proof is presented as follows.

According to (2.12) and (2.18), the modulation signal v_{Maz} is as follows:

$$v_{\text{Maz}} = V_M \cdot \sin \omega_o t + \frac{V_M}{6} \cdot \sin 3\omega_o t = \frac{3V_M}{2} \cdot \sin \omega_o t - \frac{2V_M}{3} \sin^3 \omega_o t \quad (2.19)$$

According to (2.19), it can be derived that the peak of v_{Maz} locates at $\omega_o t = \pi/3$ or $2\pi/3$. If the amplitude of v_{Maz} is set to equal to that of v_{tri} , V_M/V_{tri} can reach 1.15, which indicates that the modulation ratio of the third harmonic injection SPWM can reach 1.15. When $M_r = 1.15$, according to (2.17), the amplitude of line voltage can attain V_{in} , which is the same as that of the single-phase full-bridge inverter. In other words, the dc voltage utilization attains 1.

From the Fourier transform theory, the expansions of v_{ao} and v_{bo} in Fig. 2.7 can be obtained, which are

$$v_{ao}(t) = \frac{M_r V_{in}}{2} \sin \omega_o t + \frac{M_r V_{in}}{12} \sin 3\omega_o t + \sum_{m=1,2,3,\dots}^{\infty} \sum_{n=0,\pm 1,\pm 2,\dots}^{\pm\infty} A_{mn} \cos(m\omega_{sw}t + n\omega_o t) \quad (2.20)$$

$$\begin{aligned} v_{bo}(t) = & \frac{M_r V_{in}}{2} \sin\left(\omega_o t - \frac{2\pi}{3}\right) + \frac{M_r V_{in}}{12} \sin 3\omega_o t \\ & + \sum_{m=1,2,3,\dots}^{\infty} \sum_{n=0,\pm 1,\pm 2,\dots}^{\pm\infty} A_{mn} \cos\left(m\omega_{sw}t + n\left(\omega_o t - \frac{2\pi}{3}\right)\right) \end{aligned} \quad (2.21)$$

where A_{mn} is the amplitude of harmonics, expressed as [1]

$$A_{mn} = \frac{2V_{in}}{m\pi} \left[\begin{aligned} & J_0(mM_r\pi/12)J_k(mM_r\pi/2) \sin[(m+k)\pi/2]|_{k=|n|} \\ & + J_0(mM_r\pi/2)J_h(mM_r\pi/12) \sin[(m+h)\pi/2]|_{3h=|n|} \\ & + \sum J_k(mM_r\pi/2)J_h(mM_r\pi/12) \sin[(m+k+h)\pi/2]|_{k+3h=|n|} \\ & + \sum J_k(mM_r\pi/2)J_h(mM_r\pi/12) \sin[(m+k+h)\pi/2]|_{k-3h=|n|} \\ & + \sum J_k(mM_r\pi/2)J_h(mM_r\pi/12) \sin[(m+k+h)\pi/2]|_{3h-k=|n|} \end{aligned} \right] \quad (2.22)$$

Same as the derivation of output phase voltage v_{aN} with SPWM in Sect. 2.2.1, the expression of v_{aN} with the third harmonic injection SPWM can be derived, expressed as

$$v_{aN}(t) = \frac{M_r V_{in}}{2} \sin \omega_o t + \sum_{m=1,2,3,\dots}^{\infty} \sum_{n=0,\pm 1,\pm 2,\dots}^{\pm \infty} \frac{4}{3} \sin^2 \frac{n\pi}{3} \cdot A_{mn} \cos(m\omega_{sw}t + n\omega_o t) \quad (2.23)$$

By comparing (2.16) and (2.23), the harmonics spectrum of the output phase voltages of three-phase inverter with the third harmonic injection SPWM can be concluded as follows:

- (1) The harmonics in the output phase voltages v_{xN} ($x = a, b, c$) only distribute at the frequencies where $m + n$ is odd. When m is odd, the harmonics only distribute at even sideband frequencies where $n = 6k \pm 2$ (k is an integer); when m is even, the harmonics only distribute at odd sideband frequencies where $n = 6k \pm 1$.
- (2) The harmonics in v_{xN} at around the carrier frequency ($n = \pm 2, \pm 4, \dots$) are the dominant harmonics, which is the major consideration of filter design.

According to (2.20) and (2.21), the output line voltage v_{ab} can be obtained as

$$\begin{aligned} v_{ab}(t) &= v_{ao}(t) - v_{bo}(t) \\ &= \frac{\sqrt{3}M_r V_{in}}{2} \sin\left(\omega_o t + \frac{\pi}{6}\right) \\ &\quad + \sum_{m=1,2,3,\dots}^{\infty} \sum_{n=0,\pm 1,\pm 2,\dots}^{\pm \infty} 2 \sin \frac{n\pi}{3} \cdot A_{mn} \cos\left(m\omega_{sw}t + n\omega_o t + \frac{\pi}{2} - \frac{n\pi}{3}\right) \end{aligned} \quad (2.24)$$

Besides (2.18), the harmonic v_z injected to the modulation sinusoidal signal can be generated from the envelope magnitude of v_{Ma} , v_{Mb} , and v_{Mc} [1], which means that the maximum magnitude of $|v_{Ma}|$, $|v_{Mb}|$ and $|v_{Mc}|$ is selected, as shown in Fig. 2.8. In detail, within $\omega_o t \in [0, \pi/6) \cup [5\pi/6, 7\pi/6) \cup [11\pi/6, 2\pi)$, $|v_{Ma}|$ is the largest one, so v_z is extracted from v_{Ma} ; Likewise, within $\omega_o t \in [\pi/6, \pi/2) \cup [7\pi/6, 3\pi/2)$, $|v_{Mb}|$ is the largest one, then v_z is extracted from v_{Mb} ; Within $\omega_o t \in [\pi/2, 5\pi/6) \cup [3\pi/2, 11\pi/6)$, $|v_{Mc}|$ is the largest one, and v_z is extracted from v_{Mc} . Due to $v_{Ma} + v_{Mb} + v_{Mc} = 0$, v_z can be expressed as follows

$$v_z = -k(\max\{v_{Ma}, v_{Mb}, v_{Mc}\} + \min\{v_{Ma}, v_{Mb}, v_{Mc}\}) \quad (2.25)$$

It also can be proved that the peak of the modulation signal v_{Maz} locates at $\omega_o t = \pi/3$ or $2\pi/3$. When k in (2.25) equals to 0.5, the dc voltage utilization can also

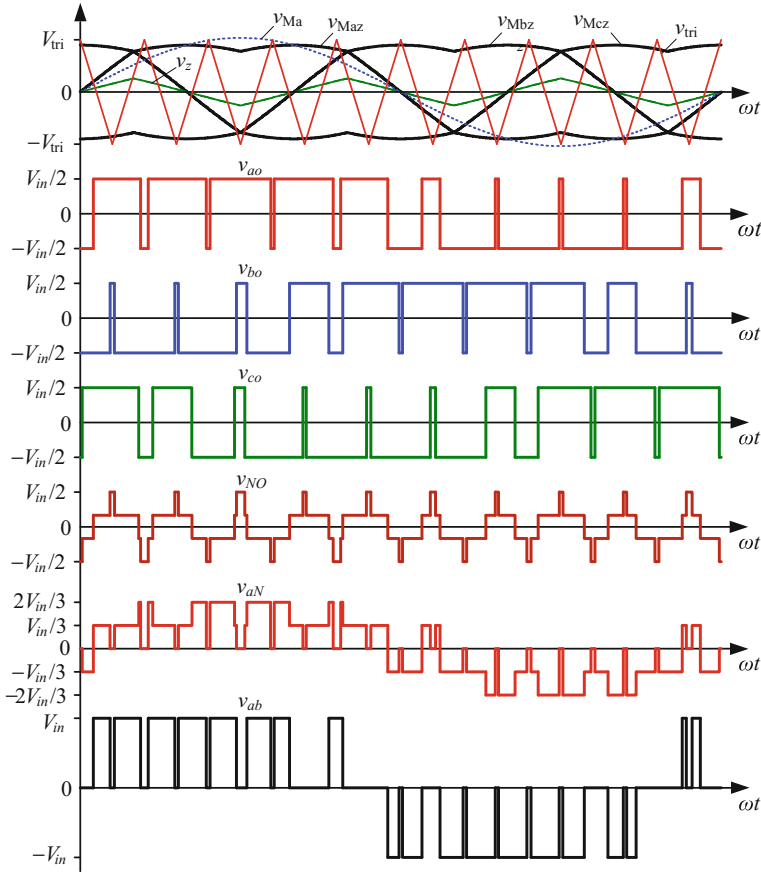


Fig. 2.8 Harmonic injection SPWM for three-phase *LCL*-type grid-connected inverter that is equivalent to SVM

attain 1. The result of harmonic injection SPWM shown in Fig. 2.8 is equivalent to the space vector modulation (SVM) [1]. Since the zero sequence component extracts directly from the modulation sinusoidal signals, the realization of the three-phase modulation signals shown in (2.25) is simple and widely used.

The amplitude A_{mn} of output harmonics voltage controlled by the harmonic injection SPWM shown in Fig. 2.8 is expressed as [2]

$$A_{mn} = \frac{4V_{in}}{m\pi^2} \left[\begin{aligned} & \frac{\pi}{6} \sin \frac{(m+n)\pi}{2} \left[J_n \left(\frac{3mM_r\pi}{4} \right) + 2 \cos \frac{n\pi}{6} J_n \left(\frac{\sqrt{3}mM_r\pi}{4} \right) \right] \\ & + \frac{1}{n} \sin \frac{m\pi}{2} \cos \frac{n\pi}{2} \sin \frac{n\pi}{6} \left[J_0 \left(\frac{3mM_r\pi}{4} \right) - J_0 \left(\frac{\sqrt{3}mM_r\pi}{4} \right) \right] \Big|_{n \neq 0} \\ & + \sum_{\substack{k=1 \\ k \neq -n}}^{\infty} \left\{ \frac{1}{n+k} \sin \frac{(m+k)\pi}{2} \cos \frac{(n+k)\pi}{2} \sin \frac{(n+k)\pi}{6} \cdot \right. \\ & \quad \left. \left[J_k \left(\frac{3mM_r\pi}{4} \right) + 2 \cos \frac{(2n+3k)\pi}{6} J_k \left(\frac{\sqrt{3}mM_r\pi}{4} \right) \right] \right\} \\ & + \sum_{\substack{k=1 \\ k \neq n}}^{\infty} \left\{ \frac{1}{n-k} \sin \frac{(m+k)\pi}{2} \cos \frac{(n-k)\pi}{2} \sin \frac{(n-k)\pi}{6} \cdot \right. \\ & \quad \left. \left[J_k \left(\frac{3mM_r\pi}{4} \right) + 2 \cos \frac{(2n-3k)\pi}{6} J_k \left(\frac{\sqrt{3}mM_r\pi}{4} \right) \right] \right\} \end{aligned} \right] \quad (2.26)$$

2.3 *LCL* Filter Design

The PWM output voltage of the grid-connected inverters contains abundant of switching harmonic components, which results in the harmonic current injecting into the grid. Therefore, a filter is required to interface between the inverter bridge and the power grid. The *LCL* filter is usually employed since it has better ability of suppressing high frequency harmonics than the *L* filter. This section will focus on the design of the *LCL* filter.

The single-phase full-bridge inverter, as shown in Fig. 2.1, could be simplified to the equivalent circuit as shown in Fig. 2.9a. Likewise, when the three-phase grid voltages are balanced, the voltage potentials of node *N* and *N'* are identical. As a result, the three-phase circuit, as shown in Fig. 2.5b, can be decoupled and each phase could be simplified to the equivalent circuit as shown in Fig. 2.9b, where $x = a, b, c$. As seen, the structures of the equivalent circuits of the single-phase and three-phase *LCL* filters are the same, so the design procedures of them are almost uniform, except that the harmonic spectrum of the imposed PWM voltages are different. In the following, the grid voltage v_g is assumed a pure sinusoidal waveform.

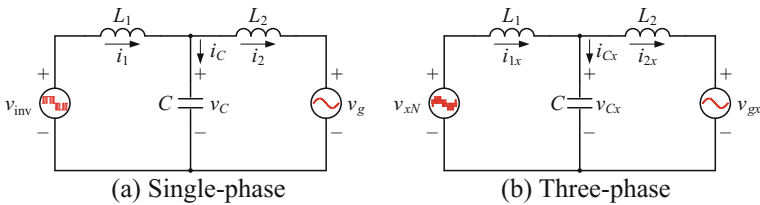


Fig. 2.9 Equivalent circuits of single-phase and three-phase *LCL*-type grid-connected inverters

2.3.1 Design of the Inverter-Side Inductor

From Figs. 2.1 and 2.5a, it can be observed that the current flowing through the filter inductor L_1 and the switches are the same. The larger the inductor current ripple is, the larger the inductor losses and higher current stress of the switches are. As a result, the conduction and switching losses will increase. Thus, the inductor current ripple should be limited.

2.3.1.1 Single-Phase Full Bridge Grid-Connected Inverter

1. Bipolar SPWM

Figure 2.10a gives the key waveforms of the single-phase full-bridge inverter with bipolar SPWM, where i_{1f} is the fundamental component in the inverter-side inductor current, and T_{sw} is the carrier period.

When $v_M > v_{tri}$, switches Q_1 and Q_4 turn on simultaneously, and the bridge output voltage $v_{inv} = V_{in}$. The voltage applied on inductor L_1 is

$$L_1 \frac{di_1}{dt} = V_{in} - v_c \quad (2.27)$$

where v_c is the filter capacitor voltage. Within one carrier period, v_c can be regarded to be constant, and $V_{in} > v_c$. So, the inductor current i_1 increases linearly, and the increment is

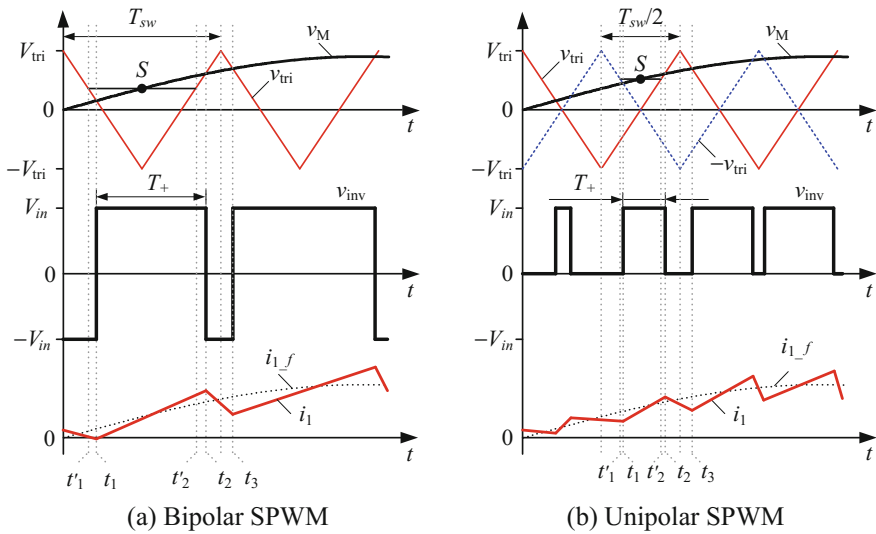


Fig. 2.10 Key waveforms of single-phase full bridge inverter

$$\Delta i_{1(+)} = \frac{V_{in} - v_C}{L_1} \cdot T_{(+)} \quad (2.28)$$

where $T_{(+)} = t_{12}$ is the time interval when Q_1 and Q_4 conduct simultaneously.

When $v_M < v_{tri}$, Q_2 and Q_3 turn on simultaneously, and $v_{inv} = -V_{in}$. The voltage across inductor L_1 is

$$L_1 \frac{di_1}{dt} = -V_{in} - v_C \quad (2.29)$$

Similarly, i_1 decreases linearly, and the decrement is

$$\Delta i_{1(-)} = \frac{V_{in} + v_C}{L_1} \cdot T_{(-)} \quad (2.30)$$

where $T_{(-)} = t_{23}$ is the time interval when Q_2 and Q_3 conduct simultaneously.

The equation for solving the intersection points of v_M and v_{tri} is transcendental, so regular sampling SPWM is usually used to calculate T_+ . In detail, a horizontal line is drawn across point S , as shown in Fig. 2.10, and it would intersect the triangle carrier at t'_1 and t'_2 . Considering the fundamental frequency is much lower than the carrier frequency, it is reasonable to have $T_{(+)} = t_{12} \approx t'_{12}$. Then, $T_{(+)}$ can be calculated, which is

$$T_{(+)} = \frac{v_M + V_{tri}}{2V_{tri}} T_{sw} = \frac{1}{2} T_{sw} (M_r \sin \omega_o t + 1) \quad (2.31)$$

Likewise, $T_{(-)}$ can be expressed as

$$T_{(-)} = T_{sw} - T_{(+)} = \frac{1}{2} T_{sw} (1 - M_r \sin \omega_o t) \quad (2.32)$$

Generally, the fundamental component in the voltage across inductors L_1 and L_2 are small, so the filter capacitor voltage v_C can be approximated to the grid voltage v_g and it equals to the fundamental component of the bridge output voltage v_{inv} , i.e.,

$$v_C \approx v_g = M_r V_{in} \sin \omega_o t \quad (2.33)$$

Substituting (2.32) and (2.33) into (2.28) and (2.30), respectively, $\Delta i_{1(+)}$ and $\Delta i_{1(-)}$ can be derived as

$$\Delta i_{1(+)} = \Delta i_{1(-)} = \frac{V_{in} T_{sw}}{2L_1} (1 - M_r^2 \sin^2 \omega_o t) \quad (2.34)$$

As seen in (2.34), either the maximum increment or decrement of the current of inductor L_1 (denoted as Δi_{1_max}) within a carrier period appears at $\sin \omega_o t = 0$, i.e., $\Delta i_{1_max} = V_{in} T_{sw} / (2L_1)$. Defining the ripple coefficient as $\lambda_{c-L1} = \Delta i_{1_max} / I_1$, where

I_1 is the rated RMS value of the fundamental component of i_1 , the minimum inductance of L_1 can be obtained as

$$L_{1_min} = \frac{V_{in}T_{sw}}{2\lambda_{c_L1}I_1} \quad (2.35)$$

In practice, λ_{c_L1} is set to be 20–30% [2].

The maximum value of L_1 could be determined from the fundamental voltage of L_1 , which is defined as v_{L1_f} . The smaller v_{L1_f} is, the lower the dc-link voltage is required. Defining the ratio of RMS values of v_{L1_f} and v_C as λ_{v_L1} , the maximum value of L_1 can be obtained, which is

$$L_{1_max} = \frac{\lambda_{v_L1}V_C}{\omega_o I_1} \approx \frac{\lambda_{v_L1}V_g}{\omega_o I_1} \quad (2.36)$$

where V_g is the RMS value of the grid voltage, and λ_{v_L1} is usually set to be about 5%.

2. Unipolar SPWM

Figure 2.10b gives the key waveforms of the single-phase full-bridge inverter with unipolar SPWM. When $v_M > v_{tri}$ and $v_M > -v_{tri}$, switches Q_1 and Q_4 turn on simultaneously, and $v_{inv} = V_{in}$. As a result, i_1 increases linearly. From Fig. 2.10b, the ratio of $T_{(+)}$ and $T_{sw}/2$ can be obtained, which is

$$\frac{T_{(+)}}{T_{sw}/2} = \frac{v_M}{V_{tri}} = M_r \sin \omega_o t \quad (2.37)$$

Substituting (2.33) and (2.37) into (2.28), the increment $\Delta i_{1(+)}$ can be derived as

$$\Delta i_{1(+)} = \frac{V_{in}T_{sw}}{2L_1}(1 - M_r \sin \omega_o t)M_r \sin \omega_o t \quad (2.38)$$

Similarly, the decrement $\Delta i_{1(-)}$ when both Q_2 and Q_3 turn on can be calculated, which is the same as (2.38).

As seen in (2.38), the maximum increment and decrement of i_1 appear when $\sin \omega_o t = 1/(2M_r)$, and $\Delta i_{1_max} = V_{in}T_{sw}/(8L_1)$. Then, the minimum of L_1 with unipolar SPWM is

$$L_1 = \frac{V_{in}T_{sw}}{8\lambda_{c_L1}I_1} \quad (2.39)$$

By Comparing of (2.35) and (2.39), it can be seen that the required L_1 with unipolar SPWM is only one-fourth of that with bipolar SPWM when that the permitted maximum increment (or decrement) of inductor current are identical. The reasons are: (1) the equivalent carrier frequency with unipolar SPWM is twice that with bipolar SPWM; (2) the bridge output voltage v_{inv} switches between V_{in} and

$-V_{in}$ when bipolar SPWM is used, while it is switched between V_{in} and 0, or 0 and $-V_{in}$ when unipolar SPWM is used.

2.3.1.2 Three-Phase Grid-Connected Inverter

Similar to the single-phase grid-connected inverter, the inverter-side inductor L_1 of the three-phase grid-connected inverter is also determined by the maximum current ripple. The fundamental voltage of L_1 is also ignored here, and the filter capacitor voltage v_{Cx} is approximated to the fundamental voltage of the inverter bridge output voltage v_{xN} , i.e., $v_{Ca} \approx (M_r V_{in}/2) \sin \omega_o t$. However, differed from the single-phase full-bridge inverter, the three-phase inverter bridge output voltage v_{xN} can output five levels, i.e., $0, \pm V_{in}/3$, and $\pm 2V_{in}/3$. As a result, the current ripple of i_{1x} ($x = a, b, c$) is more complex. In the following, a detailed analysis about the current ripple of i_{1x} will be presented. Since the voltages and currents are periodic, only the key waveforms in a quarter of one cycle, i.e., $\omega_o t \in [0, \pi/2]$ is given, as shown in Fig. 2.11.

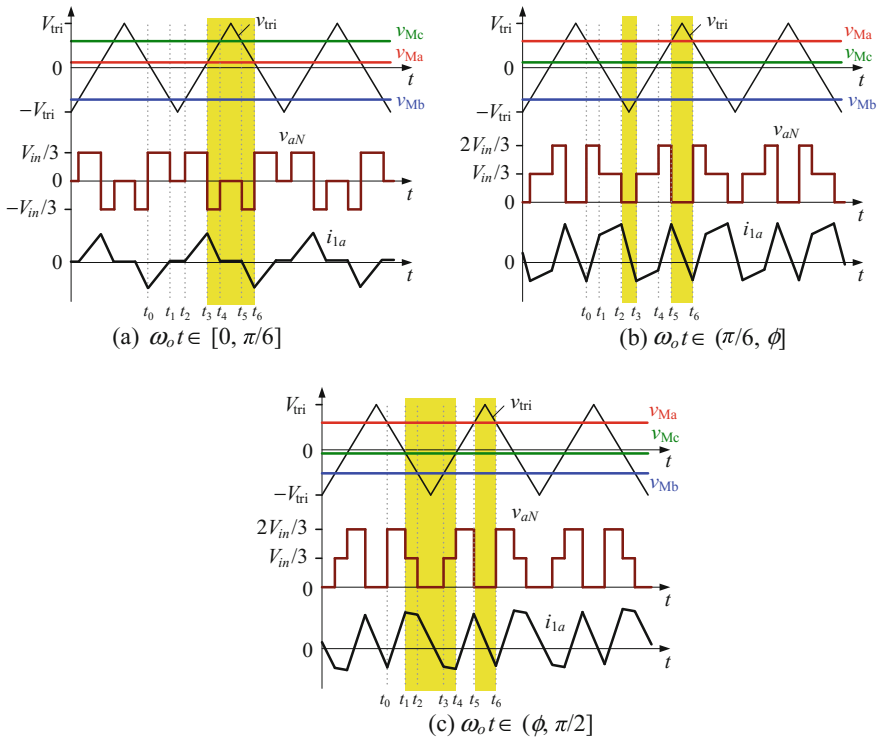


Fig. 2.11 Inverter-side inductor current of three-phase inverter

From Figs. 2.6, 2.7 and 2.8, it can be observed that no matter SPWM or harmonic injection SPWM is used, the three-phase filter capacitor voltages satisfy the relation $v_{Mc} > v_{Ma} > v_{Mb}$ within $\omega_o t \in [0, \pi/6]$. Moreover, v_{Ma} increases monotonously and reaches its maximum value at $\omega_o t = \pi/6$. Since v_{Cx} is proportional to v_{Mx} in the linear modulation region, $v_{Cc} > v_{Ca} > v_{Cb}$ is also true, and v_{Ca} increases monotonously and reaches its maximum value at $\omega_o t = \pi/6$. Thus, the maximum value of v_{Ca} equals to $(M_r V_{in}/2)\sin(\pi/6) = M_r V_{in}/4$. When SPWM or harmonic injection SPWM is used, the maximum values of v_{Ca} are $V_{in}/4$ and $1.15V_{in}/4$, respectively. Obviously, $v_{Ca} < V_{in}/3$ is always true within $\omega_o t \in [0, \pi/6]$. When $\omega_o t \in [0, \pi/6]$, i_{1a} can be divided into six sections in one carrier period, i.e., $[t_0, t_6]$, as shown in Fig. 2.11a, and three cases can be found in the six sections.

Case 1: when $t \in [t_0, t_1) \cup [t_2, t_3)$, $v_{aN} = V_{in}/3$. Since $v_{Ca} < V_{in}/3$, i_{1a} increases linearly;

Case 2: when $t \in [t_1, t_2) \cup [t_4, t_5)$, $v_{aN} = 0$. Since $v_{Ca} > 0$, i_{1a} decreases linearly;

Case 3: when $t \in [t_3, t_4) \cup [t_5, t_6)$, $v_{aN} = -V_{in}/3$. Since $v_{Ca} < V_{in}/3$, i_{1a} decreases linearly.

When $\omega_o t \in [\pi/6, \pi/2]$, $v_{Ca} > v_{Cc} > v_{Cb}$ is true, and v_{Ca} increases monotonously and reaches its maximum value at $\omega_o t = \pi/2$. The maximum value of v_{Ca} is $M_r V_{in}/2$. When SPWM or harmonic injection SPWM is used, the maximum values of v_{Ca} are $V_{in}/2$ and $1.15V_{in}/2$, respectively. Obviously, $v_{Ca} < 2V_{in}/3$ is always true within $\omega_o t \in (\pi/6, \pi/2]$. Similarly, when $\omega_o t \in (\pi/6, \pi/2]$, i_{1a} can also be divided into six sections in one carrier period, i.e., $[t_0, t_6]$, as shown in Fig. 2.11b, c, and three cases can also be found in the six sections.

Case 1: when $t \in [t_0, t_1) \cup [t_4, t_5)$, $v_{aN} = 2V_{in}/3$. Since $v_{Ca} < 2V_{in}/3$, i_{1a} increases linearly;

Case 2: when $t \in [t_1, t_2) \cup [t_3, t_4)$, $v_{aN} = V_{in}/3$. If $v_{Ca} < V_{in}/3$, i_{1a} increases linearly, as shown in Fig. 2.11b. If $v_{Ca} > V_{in}/3$, i_{1a} decreases linearly, as shown in Fig. 2.11c;

Case 3: when $t \in [t_2, t_3) \cup [t_5, t_6)$, $v_{aN} = 0$. Since $v_{Ca} > 0$, i_{1a} decreases linearly.

Defining $\omega_o t$ when $v_{Ca} = V_{in}/3$ as ϕ , yields

$$\frac{M_r V_{in}}{2} \sin \phi = \frac{V_{in}}{3} \quad (2.40)$$

Then, ϕ can be calculated as

$$\phi = \arcsin\left(\frac{2}{3M_r}\right) \quad (2.41)$$

According to (2.41), it can be obtained that only when $M_r \geq 2/3$, v_{Ca} will be possible to be larger than $V_{in}/3$, thus the case shown in Fig. 2.11c appears; and when $M_r < 2/3$, v_{Ca} will be never larger than $V_{in}/3$, thus the case shown in Fig. 2.11c does not appear.

As seen from Fig. 2.11a, i_{1a} continues decreasing within $[t_3, t_6]$. As seen from Fig. 2.11b, i_{1a} continues increasing within $[t_0, t_2]$ or $[t_3, t_5]$, and decreases within $[t_2, t_3]$ or $[t_5, t_6]$. As seen from Fig. 2.11c, i_{1a} increases within $[t_0, t_1]$ or $[t_4, t_5]$ and continues decreasing within $[t_1, t_4]$ or $[t_5, t_6]$. As mentioned above, the maximum increment and decrement of the inverter-side inductor current is identical. In the following, only the decrements of i_{1a} within $[t_3, t_6]$ shown in Fig. 2.11a, within $[t_2, t_3]$ or $[t_5, t_6]$ shown in Fig. 2.11b, and within $[t_1, t_4]$ or $[t_5, t_6]$ shown in Fig. 2.11c, will be derived. Based on these decrements, the lower limit of the inverter-side inductor can be obtained.

According to Fig. 2.11a, the decrement of i_{1a} within $[t_3, t_6]$ can be expressed as

$$\begin{aligned}\Delta i_{1a(1)} &= \left| \frac{-V_{in}/3 - v_{Ca}}{L_1} t_{34} + \frac{0 - v_{Ca}}{L_1} t_{45} + \frac{-V_{in}/3 - v_{Ca}}{L_1} t_{56} \right| \\ &= \left| \frac{V_{in}}{3L_1} (t_{36} - t_{45}) + \frac{v_{Ca}}{L_1} t_{36} \right|\end{aligned}\quad (2.42)$$

According to Fig. 2.11b, the decrements of i_{1a} within $[t_2, t_3]$ and $[t_5, t_6]$ can be, respectively, expressed as

$$\Delta i_{1a(2)} = \left| \frac{v_{Ca}}{L_1} t_{23} \right| \quad (2.43)$$

$$\Delta i_{1a(3)} = \left| \frac{v_{Ca}}{L_1} t_{56} \right| \quad (2.44)$$

According to Fig. 2.11c, the decrement of i_{1a} within $[t_1, t_4]$ can be expressed as

$$\begin{aligned}\Delta i_{1a(4)} &= \left| \frac{V_{in}/3 - v_{Ca}}{L_1} t_{12} + \frac{0 - v_{Ca}}{L_1} t_{23} + \frac{V_{in}/3 - v_{Ca}}{L_1} t_{34} \right| \\ &= \left| \frac{V_{in}}{3L_1} (t_{14} - t_{23}) - \frac{v_{Ca}}{L_1} t_{14} \right|\end{aligned}\quad (2.45)$$

And the expression of the decrement of i_{1a} within $[t_5, t_6]$ is the same as (2.44). If the SPWM is used, the following relations can be obtained from Fig. 2.11.

$$\begin{cases} t_{36} = T_{sw} \cdot (V_{tri} - v_{Ma}) / 2V_{tri} \\ t_{45} = T_{sw} \cdot (V_{tri} - v_{Mc}) / 2V_{tri} \end{cases} \quad (2.46)$$

$$\begin{cases} t_{23} = T_{sw} \cdot (V_{tri} + v_{Mb}) / 2V_{tri} \\ t_{56} = T_{sw} \cdot (V_{tri} - v_{Ma}) / 2V_{tri} \end{cases} \quad (2.47)$$

$$\begin{cases} t_{14} = T_{sw} \cdot (V_{tri} + v_{Mc}) / 2V_{tri} \\ t_{23} = T_{sw} \cdot (V_{tri} + v_{Mb}) / 2V_{tri} \end{cases} \quad (2.48)$$

If the harmonic injection SPWM is used, v_{Ma} , v_{Mb} , and v_{Mc} in (2.46)–(2.48) should be replaced by v_{Maz} , v_{Mbz} , and v_{McZ} , respectively.

When the SPWM is used, v_{Ma} , v_{Mb} , and v_{Mc} given in (2.12) and $M_r = V_M/V_{tri}$ are substituted into (2.46), t_{36} and t_{45} can be calculated. Then, by substituting t_{36} , t_{45} , and $v_{Ca} \approx (M_r V_{in}/2)\sin\omega_o t$ into (2.42), $\Delta i_{1a(1)}$ will be obtained. On the base of $M_r V_{in} T_{sw}/(2L_1)$, the normalized $\Delta i_{1a(1)}$ is finally expressed as

$$\Delta i_{1_SPWM}(\omega_o t) \triangleq \frac{\Delta i_{1a(1)}}{M_r V_{in} T_{sw}/(2L_1)} = \left| \frac{1}{6} \sin \omega_o t + \frac{1}{3} \sin \left(\omega_o t + \frac{2\pi}{3} \right) - \frac{M_r}{2} \sin^2 \omega_o t \right| \quad (2.49)$$

Similarly, according to (2.12), (2.43)–(2.45), (2.47) and (2.48), the normalized $\Delta i_{1a(2)}$, $\Delta i_{1a(3)}$, and $\Delta i_{1a(4)}$ can be derived as

$$\Delta i_{2_SPWM}(\omega_o t) \triangleq \frac{\Delta i_{1a(2)}}{M_r V_{in} T_{sw}/(2L_1)} = \left| \sin \omega_o t \left[\frac{1}{2} + \frac{M_r}{2} \sin \left(\omega_o t - \frac{2\pi}{3} \right) \right] \right| \quad (2.50)$$

$$\Delta i_{3_SPWM}(\omega_o t) \triangleq \frac{\Delta i_{1a(3)}}{M_r V_{in} T_{sw}/(2L_1)} = \left| \sin \omega_o t \left(\frac{1}{2} - \frac{M_r}{2} \sin \omega_o t \right) \right| \quad (2.51)$$

$$\begin{aligned} \Delta i_{4_SPWM}(\omega_o t) &\triangleq \frac{\Delta i_{1a(4)}}{M_r V_{in} T_{sw}/(2L_1)} \\ &= \left| \frac{2}{3} \sin \left(\omega_o t + \frac{2\pi}{3} \right) - \frac{1}{6} \sin \omega_o t - \frac{M_r}{2} \sin \omega_o t \sin \left(\omega_o t + \frac{2\pi}{3} \right) \right| \end{aligned} \quad (2.52)$$

Same as the above calculation procedure for the SPWM, when the harmonic injection SPWM is used, the normalized $\Delta i_{1a(1)}$, $\Delta i_{1a(2)}$, $\Delta i_{1a(3)}$, and $\Delta i_{1a(4)}$ can be derived, expressed as

$$\Delta i_{1_HI-SPWM}(\omega_o t) \triangleq \frac{\Delta i_{1a(1)}}{M_r V_{in} T_{sw}/(2L_1)} = \left| \frac{1}{6} \sin \omega_o t + \frac{1}{3} \sin \left(\omega_o t + \frac{2\pi}{3} \right) - \frac{3M_r}{4} \sin^2 \omega_o t \right| \quad (2.53)$$

$$\begin{aligned} \Delta i_{2_HI-SPWM}(\omega_o t) &\triangleq \frac{\Delta i_{1a(2)}}{M_r V_{in} T_{sw}/(2L_1)} \\ &= \left| \sin \omega_o t \left[\frac{1}{2} + \frac{M_r}{2} \sin \left(\omega_o t - \frac{2\pi}{3} \right) + \frac{M_r}{4} \sin \left(\omega_o t + \frac{2\pi}{3} \right) \right] \right| \end{aligned} \quad (2.54)$$

$$\begin{aligned}\Delta i_{3_HI_SPWM}(\omega_o t) &\triangleq \frac{\Delta i_{1a(3)}}{M_r V_{in} T_{sw} / (2L_1)} \\ &= \left| \sin \omega_o t \left[\frac{1}{2} - \frac{M_r}{2} \sin \omega_o t - \frac{M_r}{4} \sin \left(\omega_o t + \frac{2\pi}{3} \right) \right] \right| \end{aligned} \quad (2.55)$$

$$\begin{aligned}\Delta i_{4_HI_SPWM}(\omega_o t) &\triangleq \frac{\Delta i_{1a(4)}}{M_r V_{in} T_{sw} / (2L_1)} \\ &= \left| \frac{2}{3} \sin \left(\omega_o t + \frac{2\pi}{3} \right) - \frac{1}{6} \sin \omega_o t - \frac{3M_r}{4} \sin \omega_o t \sin \left(\omega_o t + \frac{2\pi}{3} \right) \right| \end{aligned} \quad (2.56)$$

Note that the harmonic injection SPWM is equivalent to SVM, the discussion of the inverter-side inductor current ripple with SVM is not repeated here.

Since $\sin \omega_o t = -\sin(\omega_o t - 2\pi/3) - \sin(\omega_o t + 2\pi/3)$, by substituting it into (2.55), it is easy to find that $\Delta i_{2_HI_PWM} = \Delta i_{3_HI_PWM}$.

According to (2.49)–(2.52), the curves of $\Delta i_{1_SPWM}(\omega_o t)$, $\Delta i_{2_SPWM}(\omega_o t)$, $\Delta i_{3_SPWM}(\omega_o t)$, and $\Delta i_{4_SPWM}(\omega_o t)$ are depicted, as shown in Fig. 2.12a. According to (2.53)–(2.56), the curves of $\Delta i_{1_HI_SPWM}(\omega_o t)$, $\Delta i_{2_HI_SPWM}(\omega_o t)$, $\Delta i_{3_HI_SPWM}(\omega_o t)$, and $\Delta i_{4_HI_SPWM}(\omega_o t)$ are depicted, as shown in Fig. 2.12b. From Fig. 2.12, the maximum value of the inverter-side inductor current ripple can be obtained. Thus, when the current ripple coefficients λ_{c_L1} are given, the lower limits of L_1 can be determined. In addition, the maximum value of L_1 can also be calculated from (2.36). According to the lower and upper limits of L_1 , the value of L_1 can be properly selected.

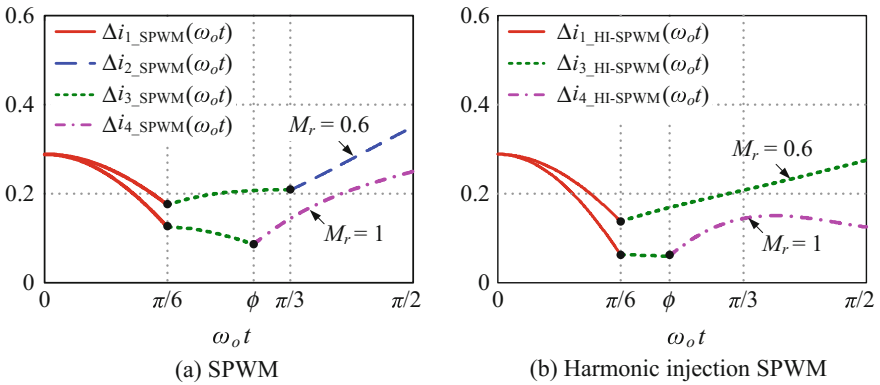


Fig. 2.12 Curves of inverter-side inductor current ripple

2.3.2 Filter Capacitor Design

The filter capacitor will lead to reactive power. The larger the capacitance is, the higher the reactive power is introduced, and also the larger the current flows through inductor L_1 and the power switches [3]. Thus, the conduction loss of the switches will increase. Defining λ_C as the ratio of the reactive power introduced by the filter capacitor to the rated output active power of the grid-connected inverter, the maximum value of filter capacitor could be expressed as

$$C = \lambda_C \cdot \frac{P_o}{\omega_o V_g^2} \quad (2.57)$$

where P_o is the rated output active power of single-phase full-bridge inverter or the rated output active power of one phase for three-phase full-bridge inverter. In practice, λ_C is usually recommended to be about 5% [4].

2.3.3 Grid-Side Inductor Design

According to Fig. 2.9a, the transfer function of the grid current i_2 to the inverter bridgeoutput voltage v_{inv} can be obtained, which is

$$G_{LCL}(s) \triangleq \frac{i_2(s)}{v_{inv}(s)} = \frac{1}{L_1 L_2 C s^3 + (L_1 + L_2)s} = \frac{1}{(L_1 + L_2)s} \cdot \frac{\omega_r^2}{s^2 + \omega_r^2} \quad (2.58)$$

where ω_r is the resonance angular frequency, which is

$$\omega_r = \sqrt{\frac{L_1 + L_2}{L_1 L_2 C}} \quad (2.59)$$

The expression of $G_{LCL}(s)$ for three-phase grid-connected inverter is the same as (2.58).

After the inverter-side inductor and the filter capacitor are determined, the grid-side inductor L_2 could be designed according to the harmonic restriction standards such as IEEE Std. 929-2000 and IEEE Std. 1547-2003 [5, 6]. Table 2.1 lists the current harmonic restriction, including the limits on individual harmonics and the limit on the total harmonics distortion (THD) of the injected grid current. If the specifications of the grid-connected inverter is given, the spectrum of v_{inv} can be calculated from (2.4) or (2.7), from which the angular frequency ω_h and amplitude $|v_{inv}(j\omega_h)|$ of the dominant harmonics can be obtained. Substituting the obtained ω_h and $|v_{inv}(j\omega_h)|$ into (2.59), yields

Table 2.1 Maximum harmonics limits of grid current

Harmonic order h (odd harmonic) ^a	$h < 11$	$11 \leq h < 17$	$17 \leq h < 23$	$23 \leq h < 35$	$35 \leq h$	THD
Proportion to the rated grid-connected current (%)	4.0	2.0	1.5	0.6	0.3	5.0

^aThe allowable maximum limits of even harmonics is 25% of those of odd harmonics in the table

$$\frac{|i_2(j\omega_h)|}{|v_{\text{inv}}(j\omega_h)|} = \frac{1}{|L_1 L_2 C(j\omega_h)^3 + j\omega_h(L_1 + L_2)|} \quad (2.60)$$

According to the spectrum of the inverter bridge output voltage v_{inv} , the angular frequency ω_h and harmonic order h of the dominant harmonics can be determined. Then, according to (2.60), Table 2.1, and the expected harmonics proportion λ_h , the minimum value of L_2 can be obtained, which is

$$L_2 = \frac{1}{L_1 C \omega_h^2 - 1} \cdot \left(L_1 + \frac{|V_{\text{inv}}(j\omega_h)|}{\omega_h \lambda_h I_2} \right) \quad (2.61)$$

where $V_{\text{inv}}(j\omega_h)$ and I_2 are the RMS value of the inverter bridge output voltage and the rated injected grid current, respectively. If three-phase grid-connected inverter is used, $V_{\text{inv}}(j\omega_h)$ in (2.60) and (2.61) is replaced by $V_{aN}(j\omega_h)$.

After L_1 , C and L_2 are determined, the simulation or experimental validations is conducted to check whether the individual harmonics and the THD of the grid current satisfy the restriction shown in Table 2.1 or not.

2.4 Design Examples for *LCL* Filter

To validate the above design methods, two prototypes are designed, where single-phase full-bridge grid-connected inverter is controlled by the unipolar SPWM, and three-phase grid-connected inverter is controlled by the harmonic injection SPWM. The specifications of the single-phase full-bridge grid-connected inverter are as follows: the dc input voltage is 360 V, the rated power is 6 kW, the carrier frequency is 10 kHz, and the grid voltage is 220 V/50 Hz. The specifications of the three-phase grid-connected inverter are as follows: the dc input voltage is 700 V, the rated power is 20 kW, the carrier frequency is 10 kHz, and the grid voltage is 380 V/50 Hz.

2.4.1 Single-Phase LCL Filter

Setting the inductor current ripple coefficient λ_{c_L1} to 30%, and substituting the corresponding parameters into (2.39), the minimum value of L_1 is calculated as 550 μH . Defining the ratio of the RMS value of the fundamental voltage of L_1 to that of the capacitor voltage as λ_{v_L1} , and assuming $\lambda_{v_L1} = 5\%$, the maximum value of L_1 is calculated from (2.36), which is 1.28 mH. Finally, $L_1 = 600 \mu\text{H}$ is chosen.

Setting $\lambda_C = 3\%$ and substituting $P_o = 6 \text{ kW}$, $V_g = 220 \text{ V}$, and $f_o = 50 \text{ Hz}$ into (2.58), yields $C < 12 \mu\text{F}$. Here, $C = 10 \mu\text{F}$ is chosen.

Assuming that the output power factor (PF) of the grid-connected inverter equals to 1, the fundamental RMS value of i_{L1} could be calculated, i.e., $I_1 = \sqrt{I_C^2 + I_2^2} = \sqrt{(\omega_o C \cdot V_g)^2 + I_2^2} = 27.28 \text{ (A)}$. According to the dc input voltage and the magnitude of grid voltage, the modulation ratio can be obtained, which is $M_r = 311/360 = 0.86$. By substituting $M_r = 0.86$ into (2.7), the spectrum of the bridge output voltage v_{inv} can be depicted, as shown in Fig. 2.13. As seen, the dominant harmonics locate at $f_h = 19.95 \text{ kHz}$ and 20.05 kHz , and the corresponding $|V_{\text{inv}}(j2\pi f_h)|/V_{\text{in}} = 28\%$. As long as these dominant harmonics in i_2 are attenuated to satisfy the aforementioned standards, the other harmonics in i_2 will naturally satisfy the standards. Since the orders of the dominant harmonics are higher than 33, the required current harmonic proportion λ_h should be less than 0.3%. Setting $\lambda_h = 0.2\%$, and substituting $I_1 = 27.28 \text{ A}$, $|V_{\text{inv}}(j2\pi f_h)|/V_{\text{in}} = 28\%$, $V_{\text{in}} = 360 \text{ V}$, $L_1 = 600 \mu\text{H}$, $C = 10 \mu\text{F}$, $\omega_h = 2\pi \times 19,950$, and $\lambda_h = 0.2\%$ into (2.61) leads to $L_2 = 164 \mu\text{H}$. Finally, $L_2 = 150 \mu\text{H}$ is selected. The final single-phase LCL filter parameters are listed in Table 2.2.

Figure 2.14 shows the simulation results. In Fig. 2.14a, the waveforms from top to bottom are the inverter-side inductor current i_1 , the grid current i_2 , the capacitor current i_C and its fundamental component, respectively. In Fig. 2.14b, the waveforms from top to bottom are the inverter bridge output voltage v_{inv} , the spectrums

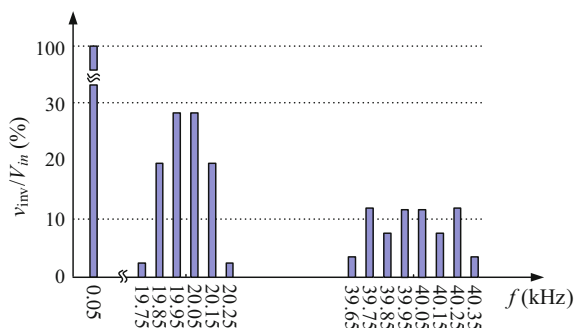
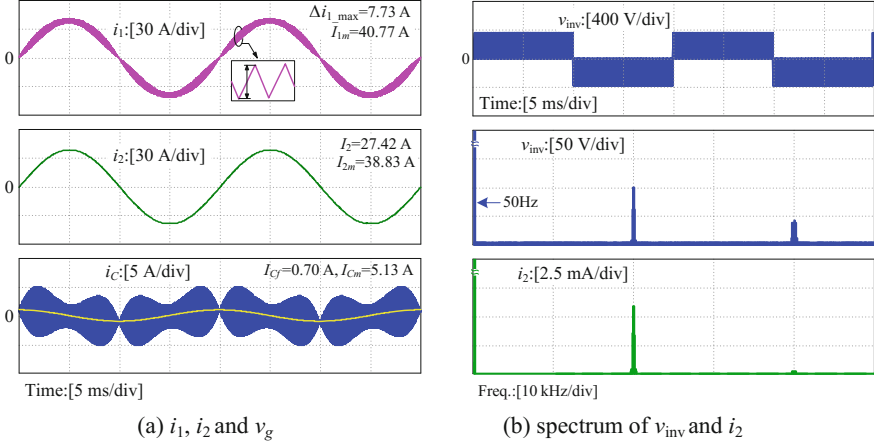


Fig. 2.13 Calculated spectrum of v_{inv} in single-phase LCL-type grid-connected inverter with unipolar SPWM

Table 2.2 Parameters of single-phase *LCL*-type full-bridge grid-connected inverter

Parameter	Symbol	Value	Parameter	Symbol	Value
Input voltage	V_{in}	360 V	Switching frequency	f_{sw}	10 kHz
Grid voltage	V_g	220 V	Inverter-side inductor	L_1	600 μH
Output power	P_o	6 kW	Filter capacitor	C	10 μF
Fundamental frequency	f_o	50 Hz	Grid-side inductor	L_2	150 μH

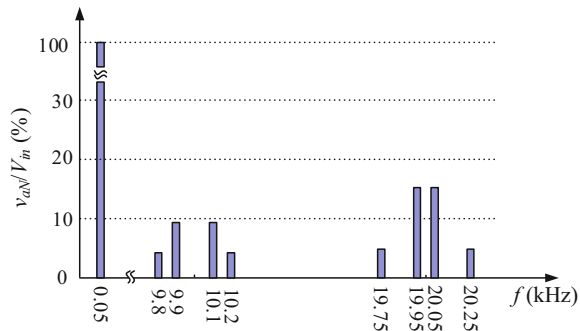
**Fig. 2.14** Simulation results of single-phase full-bridge grid-connected inverter

of v_{inv} and i_2 , respectively. The maximum current ripple of i_1 is 7.73 A, and the RMS value of i_1 is 27.28 A. As a result, $\Delta i_{1_max}/I_1 = 28\%$. As seen from Fig. 2.14b, the maximum harmonic magnitude of v_{inv} is 100 V, and it appears at 19.95 kHz. The magnitude of the harmonic is 27.8% of V_{in} , which is agreement with the calculated results shown in Fig. 2.13. Through the *LCL* filter, the magnitude of the current harmonic in i_2 at 19.95 kHz is suppressed below 0.06 A, which is 0.15% of the rated injected grid current; and the THD of i_2 is 0.8%. Clearly, both the single harmonic and THD satisfy the restriction standards, which validate the effectiveness of the design procedure for single-phase *LCL* filter.

2.4.2 Three-Phase *LCL* Filter

According to (2.23), the modulation ratio can be obtained as $M_r = 220\sqrt{2}/350 = 0.888$. As observed from Fig. 2.12b, the maximum current ripple of the inverter-side inductor appears at $\omega_o t = 0$. Setting the inductor current ripple coefficient $\lambda_{c_L1} = 30\%$, and according to Eq. (2.49), the minimum value of

Fig. 2.15 Calculated spectrum of v_{aN} when harmonic injection SPWM is used



L_1 is calculated as 988 μH . Assuming $\lambda_{v_{L1}} = 5\%$, the maximum value of L_1 is calculated from (2.36), which is 1.16 mH. So, $L_1 = 1$ mH is selected.

Setting $\lambda_C = 5\%$ and substituting $P_o = 20/3$ kW, $V_g = 220$ V, and $f_o = 50$ Hz into (2.58) yields $C < 22$ μF . Here, $C = 20$ μF is selected.

Assuming PF = 1, the fundamental RMS value of i_{L1} could be calculated as $I_1 = 30.31$ A. Substituting $M_r = 0.888$ into (2.26), the spectrum of the output phase voltage v_{aN} is depicted, as shown in Fig. 2.15. As seen, the dominant harmonics locate at $f_h = 9.9$ kHz and 10.1 kHz, where $|V_{aN}(j2\pi f_h)|/V_{in} = 17.6\%$. Likewise, as long as these dominant harmonics in i_2 are attenuated to satisfy the aforementioned standards, the other harmonics in i_2 will naturally satisfy the standards. Since the orders of these dominant harmonics are higher than 33, so the required λ_h should be less than 0.3%. Here, setting $\lambda_h = 0.15\%$, and substituting $I_1 = 30.31$ A, $|V_{inv}(j2\pi f_h)|/V_{in} = 17.6\%$, $V_{in} = 360$ V, $L_1 = 1$ mH, $C = 20$ μF , $\omega_h = 2\pi \times 9900$ and $\lambda_h = 0.15\%$ into (2.61), produces $L_2 = 301$ μH . Finally, $L_2 = 300$ μH is selected. The final three-phase *LCL* filter parameters are listed in Table 2.3.

Figure 2.16 shows the simulation results with the prototype parameters of Table 2.3. In Fig. 2.16a, the waveforms from top to bottom are the inverter-side inductor current i_{1a} , the injected grid current i_{2a} , the capacitor current i_{Ca} and its fundamental component, respectively. In Fig. 2.16b, the waveforms from top to bottom are the output phase voltage v_{aN} , the spectrums of v_{aN} and i_{2a} , respectively. The maximum current ripple of i_{1a} is 9.5 A, and the RMS value of i_1 is 30.31 A. As a result, $\Delta i_{1\text{-max}}/I_1 = 31.4\%$. As seen from Fig. 2.16b, the maximum harmonic magnitude in v_{aN} appears at 9.9 kHz and it is about 60 V, which is 17.1% of $V_{in}/2$ and in agreement with the calculated results shown in Fig. 2.15. Through the *LCL*

Table 2.3 Parameters for three-phase *LCL*-type full-bridge grid-connected inverter

Parameter	Symbol	Value	Parameter	Symbol	Value
Input voltage	V_{in}	700 V	Switching frequency	f_{sw}	10 kHz
Grid voltage	V_{gab}	380 V	Inverter-side inductor	L_1	1 mH
Output power	P_o	20 kW	Filter capacitor	C	20 μF
Fundamental wave frequency	f_o	50 Hz	Grid-side inductor	L_2	300 μH

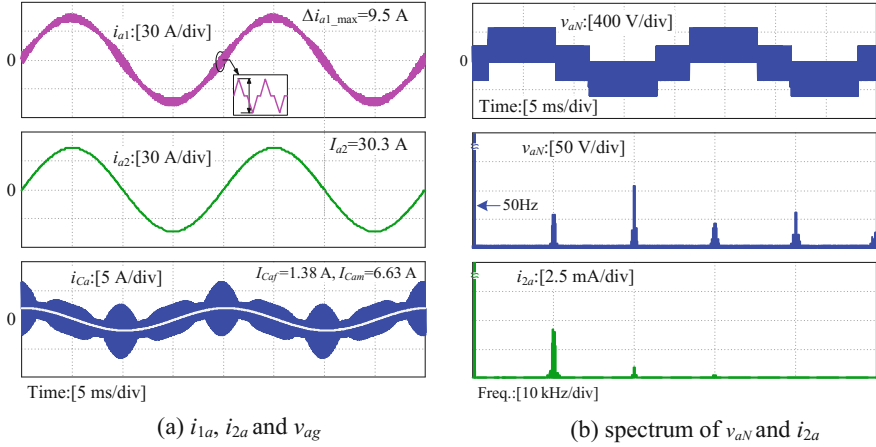


Fig. 2.16 Simulation results of three-phase grid-connected inverter

filter, the current harmonic magnitude of i_2 at 9.9 kHz is suppressed below 0.05 A, which accounts for 0.13% of the rated injected grid current. The THD of i_2 is 0.8%. Both the single harmonics and THD satisfy the restriction standards, which validate the design procedure for three-phase *LCL* filter.

2.5 Summary

In this chapter, the design procedure of *LCL* filter is presented. The Fourier series expansions of the inverter bridge output voltage of single- and three-phase *LCL*-type grid-connected inverter with different PWM schemes are derived for the purpose of determining the dominant harmonics which needs to be suppressed. The harmonic spectrum shows that for single-phase inverter, the dominant harmonics with the bipolar SPWM distribute around the carrier frequency, whereas those with the unipolar SPWM distribute around twice the carrier frequency. For the three-phase inverter, the dominant harmonics with both the SPWM and the harmonic injection SPWM distribute around the carrier frequency. Considering the permitted current ripple of the inverter-side inductor, the allowable reactive power introduced by the filter capacitor, and the maximum harmonic limit of the grid current, the filter parameters can be determined. The design procedure for the *LCL* filter is given as follows:

- (1) By limiting the maximum inductor current ripple in one cycle and the fundamental voltage on the inductors, the lower and upper limits of the inverter-side inductor is obtained, from which, a proper inverter-side inductor can be selected.

- (2) According to the maximum reactive power introduced by the filter capacitor, the upper limit of the filter capacitor can be obtained.
- (3) By limiting the single harmonic of the grid current in accord with the restriction standards, the minimum value of the grid-side inductor can be determined, from which, the proper grid-side inductor can be selected.

The *LCL* filter design procedure is verified by simulations.

References

1. Holmes, D.G., Lipo, T.A.: Pulse Width Modulation for Power Converters: Principles and Practice. IEEE Press & Wiley, New York, NY (2003)
2. Holmes, D.G.: A general analytical method for determining the theoretical harmonic components of carrier based PWM strategies. In: Proceeding of Annual Conference of IEEE Industry Applications Society, pp. 1207–1214 (1998)
3. Jalili, K., Bernet, S.: Design of *LCL* filters of active-front-end two-level voltage-source converters. IEEE Trans. Ind. Electron. **56**(5), 1674–1689 (2009)
4. Liserre, M., Blaabjerg, F., Hansen, S.: Design and control of an *LCL*-filter-based three-phase active rectifier. IEEE Trans. Ind. Appl. **41**(5), 1674–1689 (2005)
5. IEEE Std. 929: *IEEE Recommended Practice for Utility Interface of Photovoltaic (PV) Systems* (2000)
6. IEEE Std. 1547: *IEEE Standard for Interconnecting Distributed Resources with Electric Power Systems* (2003)

Control Techniques for LCL-Type Grid-Connected
Inverters

Ruan, X.; Wang, X.; Pan, D.; Yang, D.; Li, W.; Bao, C.
2018, XXII, 305 p. 203 illus., 190 illus. in color.,
Hardcover

ISBN: 978-981-10-4276-8